Time evolution of dehydration-induced stick-slip behaviors of simulated bassanite gouges

M. Kawabata[1], R. Shiraishi[1], J. Muto[1], H. Nagahama[1], Y. Sasaki[2], and M. Iwasaki[3]

[1]Department of Earth Sciences, Graduate School of Science, Tohoku University, 6-3 Aramaki-Aza-Aoba, Aoba-ku, Sendai, Miyagi, 980-8578, Japan

[2]Kaijo Junior and Senior High School, 3-6-1 Okubo, Shinjuku-ku, Tokyo, 169-0072, Japan

[3]Dia Nippon Engineering Consultants Co., Ltd., 2-272-3 Yoshinocho, Saitamashi Kitaku, Saitama, 331-0811, Japan

Corresponding author: Rei Shiraishi (rei.shiraishi.b5@tohoku.ac.jp)

Key Points:

- During friction experiments on simulated bassanite gouges, pore pressure occurred due to the dehydration of bassanite.
- The Avrami kinetics of dehydration bassanite represented the information on pore structures.
- The amount of slip of deformation was controlled by dehydration kinetics of hydrous minerals.

Abstract

Pore fluid pressure generated by dehydration of hydrous minerals can trigger deep and intermediate-depth earthquakes. To investigate its effect on frictional behaviors, we conducted friction experiments on simulated bassanite gouges and observed the stress drops and recurrence intervals of stick-slip events decreased over time under 200 MPa and 110 °C. Microstructural observations indicates that gouges deformed under room temperature shows the development of numerous shear bands including Riedel shears. On the other hand, a sample deformed under 200 MPa and 110 °C had few Riedel shear planes, indicative of the elevated pore fluid pressure suppressing the development of shear planes. We derived time function of dehydration-driven pore fluid pressure evolution using Avrami kinetics. Because of the mathematical similarity of Avrami equation and the fractal geometry, our result shows that the kinetics-driven pore fluid pressure evolution controlled the stick-slip behaviors of the basanite gouges under dehydration.

Plain Language Summary

The dehydration of hydrous minerals is one of the mechanisms of deep and intermediate-depth earthquakes in the subduction zone. We conducted friction experiments on simulated calcium sulfate hemihydrate gouges. Pore fluid pressure was observed as a result of dehydration of hydrous minerals. We showed that the dehydration kinetics of hydrous minerals controlled the stick-slip behavior. We expect to estimate the seismogenesis of deep and intermediate-depth earthquakes in the subduction zone based on dehydration kinetics.

1 Introduction

Reducing effective pressure, and resulting in dehydration embrittlement has been proposed as one of the mechanisms of deep and intermediate-depth earthquakes in the subduction zone (e.g., Raleigh & Paterson, 1965; Kirby, 1995; Brantut et al., 2012; Shiraishi et al., 2022). This mechanism indicates that subducting hydrous minerals dehydrated at elevated temperature and pressure generate pore fluid pressure, and reduce failure strengths (e.g., Raleigh & Paterson, 1965; Yamasaki & Seno, 2003). However, whether dehydration of hydrous minerals causes earthquakes is still under debate (Chernak & Hirth, 2011; Procter & Hirth, 2015).

Many deformation experiments for gypsum ($CaSO_4 \cdot 2H_2O$) have been conducted, because it can dehydrate under relatively low temperature and low pressure and can easily reproduce the dehydration process of hydrous minerals in the laboratory (e.g., Milsch & Scholz, 2005; Olgaard & Wong, 1995). Leclère et al. (2016) performed triaxial deformation experiments using gypsum, and directly measured the variation of pore fluid pressure, which demonstrated the decrease in strength due to dehydration-derived pore fluid pressure.

To study the dehydration kinetics of hydrous minerals, Perrillat et al. (2005) conducted *in-situ* heating experiments using antigorite, a major mineral within subduction zones. The *in-situ* analysis suggested that dehydration of antigorite obey the kinetic equation, Avrami theory. Additionally, Chollet et al. (2009) also studied the dehydration kinetics of talc using dehydration experiments conducted under high pressure and high temperature and showed that estimated dehydration rate based on the kinetics data was greater than viscous relaxation rate of surrounding materials. Since dehydration of hydrous minerals proceeds at a rate greater than the

viscous relaxation rate, the released water generates pore fluid pressure, which can reduce mechanical strength and trigger intraplate earthquakes.

By combining two important elements, pore fluid pressure and dehydration kinetics, that have been studied based on dehydration reactions of hydrous minerals, it is expected that time variation of dehydration-derived pore fluid pressure can be quantitatively described. In this study, we represent time evolution of pore fluid pressure, based on shear deformation experiments of simulated bassanite (dehydrated gypsum, $CaSO_4 \cdot 0.5H_2O$) gouges associated with dehydration instability. Under the assumption that pore fluid pressure was linearly proportional to dehydration ratio, the behavior of pore fluid pressure calculated from the experimental results fits well with Avrami kinetics.

2 Materials and Methods

We conducted triaxial shear deformation experiments using the high pressure gas confining apparatus (PRETECH Co., LTD., Japan) installed at Tohoku University (Onuma et al., 2011; Hirata et al., 2014; Jayawickrama et al., 2021). Bassanite ($CaSO_4 \cdot 0.5H_2O$) powders were used as the starting materials. To begin with, we dried gypsum($CaSO_4$) under 60 °C for more than a month in order to eliminate humidity. X-ray diffraction (XRD) revealed that the sample after drying turned into bassanite. As gypsum is no longer stable over 40 °C in the atmosphere, the phase transition from gypsum to bassanite could have occurred. The samples were cylindrical cores (radius, 10 mm; height, 40 mm) with bassanite gouges (thickness of gouge, 0.5 mm; particle size, 63 ~ 125 μm) sandwiched between gabbroic forcing blocks at an axial angle of 35 degrees. We covered the samples with a heat shrinkable tube indicating that the experiments were conducted under undrained conditions. Before deformation experiments, all samples except the one under 10MPa and room temperature (RT) were precompacted at room temperature for 30 minutes. In the precompaction, confining pressure was increased to 200 MPa without loading, and then differential stress of 200 MPa was applied. In our experiments, we installed a load cell on the lower piston of the assembly and a high-precision laser displacement transducer on the upper piston to measure the load and displacement, respectively. The experimental conditions were eight combinations of confining pressures and temperatures: 10 MPa and RT, 50 MPa and RT, 100 MPa and RT, 150 MPa and RT, 200 MPa and RT, 200 MPa and 70 °C, 200 MPa and 110 °C, and 200 MPa and 110-180 °C (see Table S1 for strain rate). We set the 200 MPa and maximum 180 °C condition to ensure that gypsum series can completely dehydrate. After the experiments, we made thin sections using water-insoluble grinding oil to observe microstructures using scanning electron microscope (SEM, JEOL 7001F).

3 Results

Figure 1 and S1 show stress-strain curves obtained from triaxial shear deformation experiments on bassanite gouge samples under confining pressures up to 200 MPa and temperatures ranging from room temperature to 180 °C. The experiments conducted under RT with various confining pressures show the increase in peak strengths with confining pressures. Moreover, periodic stick-slips occurred except for 10 MPa and RT condition (hereafter, 10MPa_RT), and the recurrence intervals of those slip events depended on confining pressures

(Figure 2). Additionally, the experiment conducted under high temperature but within a stability field of gypsum (200MPa_70°C) showed the similar behavior to the one conducted under RT.

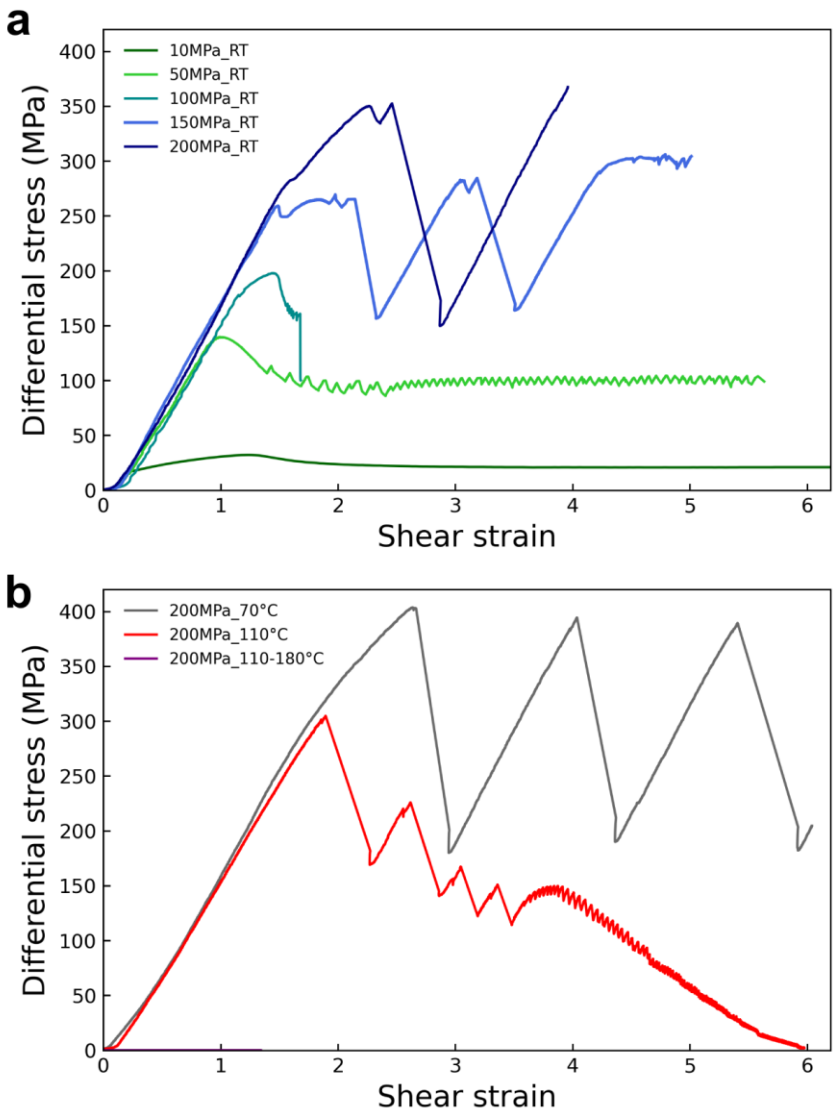

Figure 1. Stress-strain curve during triaxial shear deformation experiments under eight conditions. Temperature conditions are (**a**) room temperature (denoted as RT), and (**b**) over 70 °C. The characters of legends are confining pressure (MPa) and temperature (°C). The results under 70 °C or below showed almost constant differential stress, while the differential stress under 200MPa_110°C (red plot) remarkably decreased with strain. The differential stress under 200MPa_110-180°C was relatively almost 0 MPa.

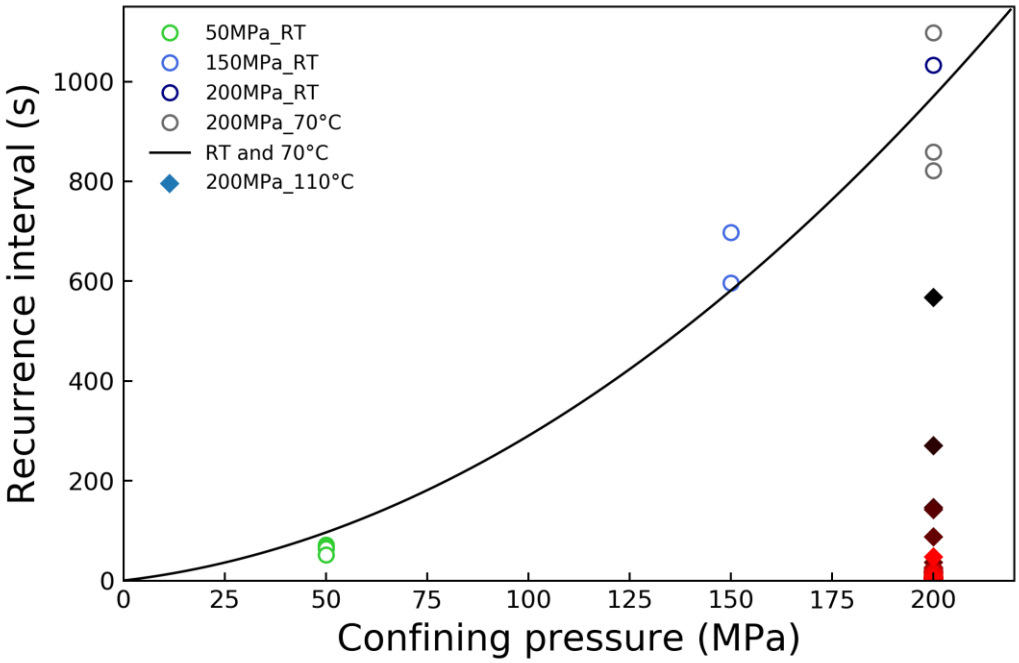

Figure 2. The relationship between confining pressure (MPa) and recurrence interval (s). Since no large sharp stress drop event was observed under 10MPa_RT and under 200MPa_110-180°C and we could not uniquely recognize recurrence interval under 100MPa_RT, we plotted the data under other five conditions. The black curve is a quadratic fitting for RT and 70 °C conditions. Regarding the data of 200MPa_110°C (diamond plot), we used gradient color scheme with black for the first stress drop event data (corresponding to shear strain of about 1.9 in Fig. 1**b**) and red for the last stress drop event data (corresponding to shear strain of about 5.9 in Fig. 1**b**). By substituting each recurrence interval under 200MPa_110°C into the derived quadratic function, we can estimate the effective pressure at each stress drop event.

The peak strengths, including the amount of stress drop and recurrence interval of slip events, decreased over time in a sample deformed under 200MPa_110°C. Moreover, there was a high positive correlation between recurrence intervals and the slip amounts of the preceding events (Figure S2). This suggests that the stick-slip behavior under 200MPa_110°C follows time-predictable recurrence model (Shimazaki & Nakata, 1980). Figure 2 shows the relationship between confining pressures P_c (MPa) and recurrence intervals Δt (s) for five experiments. We excluded the data under 10MPa_RT and 200MPa_110-180°C because we could not recognize any slip events with clear stress drops in those experiments, and we also excluded the data under 100MPa_RT because we could not uniquely recognize recurrence interval. As the experiments

conducted under 70 °C or RT indicated a positive correlation between confining pressures and recurrence intervals, we derived a regression curve from the data. Considering the negative recurrence intervals extrapolated by a linear regression, we adopted a quadratic regression curve and obtained the following equation:

$$\Delta t = aP_c^2 + bP_c, \#(1)$$

where a is 0.0195 s· MPa^{-2}, and b is 0.952 s·MPa^{-1} (R^2 = 0.957). We set the constant to 0 as the minimum of recurrence interval should be 0, consistent with the experiment conducted under 10 MPa.

X-ray diffraction (XRD) analysis for the starting material and recovered gouges revealed that the sample deformed under 200 MPa and 110-180 °C was transformed to anhydrite (dehydrated bassanite, $CaSO_4$); however, other samples including the one under 200MPa_110°C remained bassanite (Figure 3).

Representative microstructures in the recovered samples are shown in Figure 4 and S3. We recognized Riedel (R1) shear planes in samples deformed under 200MPa_RT and 200MPa_70°C (Figure 4a and 4b). In the sample deformed under 200MPa_110°C, despite multiple large stress drops, most of the identified cracks were perpendicular to the shear zone boundary (Figure 4c) and only a few Riedel shear planes existed (Figure 4d). In the sample deformed under 200MPa_110-180°C, P shear planes (oblique in the opposite direction to the Riedel shear planes) were confirmed in addition to Riedel shear planes, and some areas of the slip boundary were found to be missing.

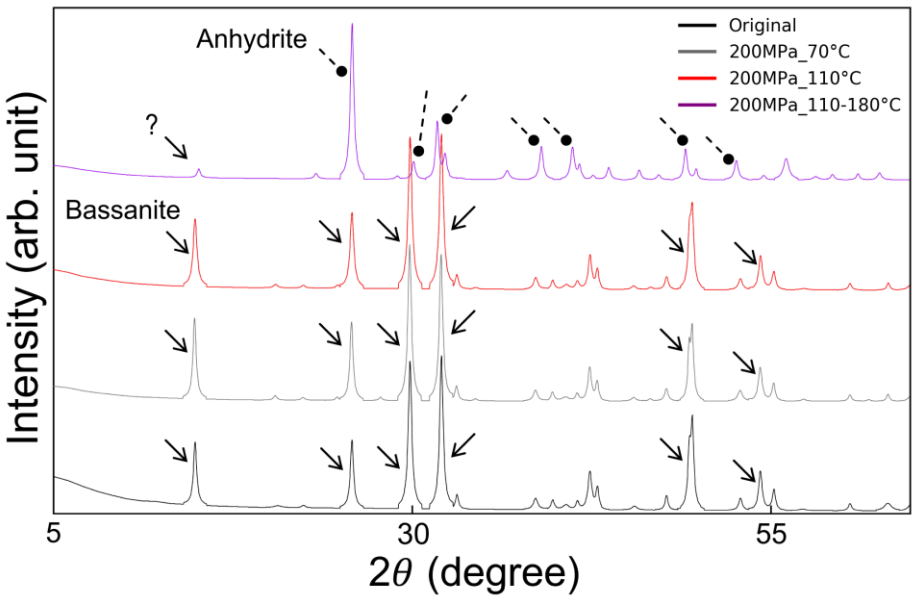

Figure 3. The results of X-ray diffraction. The arrows and dots indicate the locations of bassanite and anhydrite, respectively. The peak at about 15° of the sample deformed under 200MPa_110-180°C could not be identified. The sample under 200MPa_110-180°C was revealed as anhydrite. However, the others, including the sample under 200MPa_110°C which

showed the reduction in the amount of stress drop and recurrence interval with time, turned out to be bassanite.

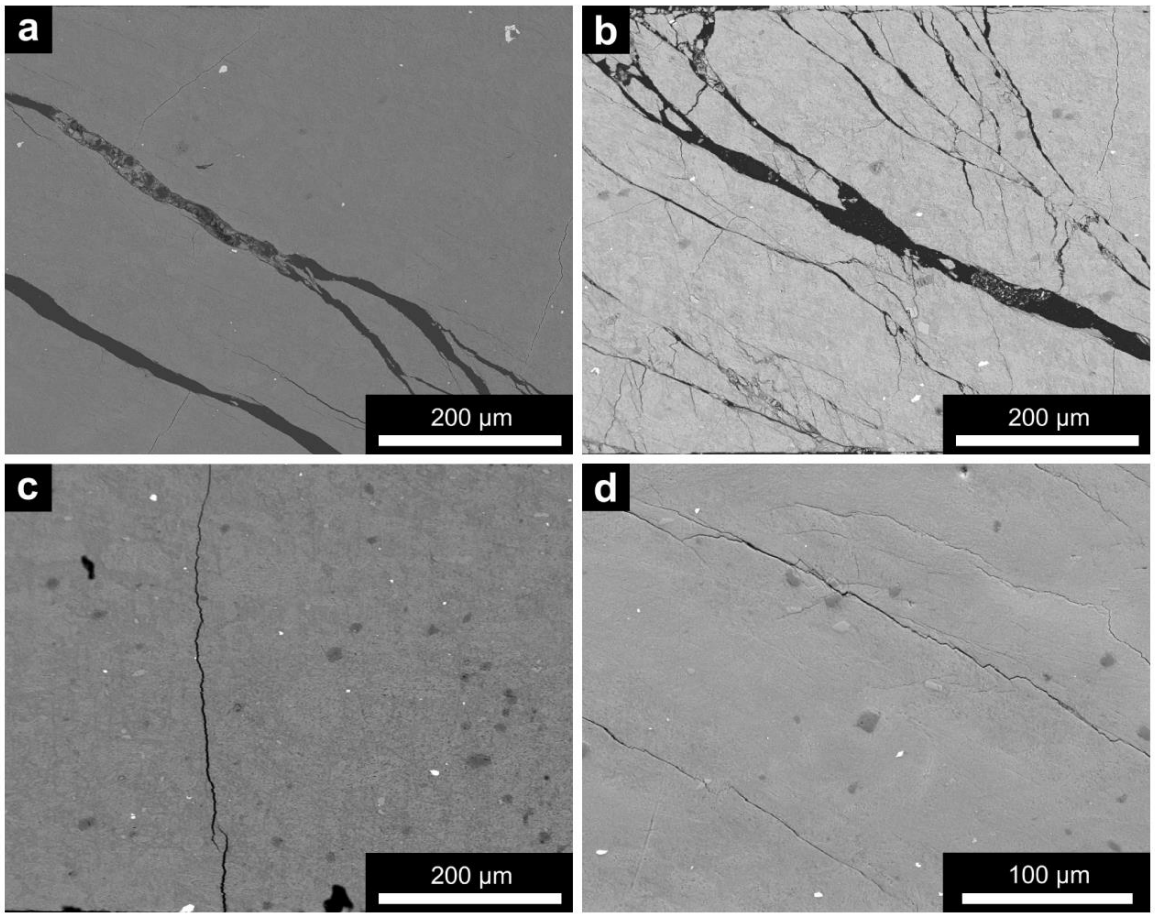

Figure 4. Microstructures of deformed samples under confining pressures of 200 MPa obtained by scanning electron microscopy. The senses of shears are dextral. The temperature conditions were RT (**a**), 70 °C (**b**), and 110 °C (**c** and **d**). Riedel shear planes have developed on the microstructures under RT (**a**) or 70 °C (**b**). Commonly observed microstructures under 110 °C were cracks perpendicular to the shear plane (**c**) although we were able to confirm a few Riedel shear planes under 110 °C (**d**).

4 Discussion

4.1 Dehydration triggering the reduction in frictional strength

In the experiment conducted under 200MPa_110°C, differential stresses and recurrence intervals gradually decreased with strain (Figure 1b) despite that the experiment was conducted under the constant confining pressure. The experiments conducted under RT showed that the recurrence intervals were dependent on confining pressures (Figure 2), which implies temporal change in effective pressure in the experiment conducted under 200MPa_110°C. XRD analysis clarified that only the sample deformed under 200MPa_110-180°C was transformed into anhydrite. In other words, the sample deformed under 200MPa_110°C did not dehydrate and remained the same as the starting material after the experiment. However, among calcium sulfate hydrates, anhydrite is the most stable above 75 °C under 200 MPa (Mirwald, 2008). Additionally, it has been clarified that anhydrite can absorb water vapor in the air to form bassanite (Tang et al., 2019). These imply that the sample deformed under 200MPa_110°C was dehydrated under the experimental condition and rehydrated again into the bassanite. Therefore, in the discussion, we first discuss the possibility of dehydration of bassanite gouges under 200MPa_110°C.

Previous experiments of simulated gouges have reported the formation of continuous Riedel (R1) shear planes (Leclère et al., 2016; Gu & Wong, 1994; Onuma et al., 2011; Hirauchi & Muto, 2015). From the friction experiment conducted under semi-undrained conditions using gypsum gouge, Leclère et al. (2016) demonstrated few Riedel shear planes under the low shear stress condition due to elevated pore fluid pressure by dehydration. Furthermore, they reported the continuous development of Riedel shear planes under fully drained condition where the elevated pore pressure escaped from the gouge and the shear stress reached its maximum. These results suggest that the elevated pore fluid pressure within the gouges inhibits the development of the localized shear planes in the gypsum gouge. Thus, scarce development of the Riedel shear planes in the sample deformed under 200MPa_110°C supports the generation of pore fluid pressure during the deformation experiment.

Since microstructural observations suggested that pore fluid pressure may have been elevated during the experiment under 200MPa_110°C, we evaluated frictional coefficients with and without pore fluid pressure. We calculated effective pressures under 200MPa_110°C by assigning the recurrence intervals in Equation (1) and derived pore fluid pressure by subtracting effective pressure from the experimental confining pressure of 200 MPa. If the pore fluid pressure is not taken into account, the strength of the sample declining gradually with time shows anomalously high frictional coefficient (> 1) with a negative cohesion (Figure 5a). However, assuming the existence of pore fluid pressure, frictional coefficients were estimated to be approximately 0.6 (Figure 5 and Table S2), which is consistent with that of previous study (Scuderi et al., 2013). This also indicates that the temporal reduction in strengths of the sample under 200MPa_110°C is attributed not to the change of physical property but the generation of pore fluid pressure. Therefore, we conclude that the gradual change in slip behavior during the experiment under 200MPa_110°C originated from the elevated pore fluid pressure controlled by

dehydration kinetics of bassanite gouges. The crystalline system of anhydrite is hexagonal for soluble anhydrite and orthorhombic for insoluble anhydrite (Freyer & Voigt, 2003). Under 200MPa_110-180°C, the crystalline system may have fully changed into insoluble anhydrite due to the rapid dehydration reaction, leading to inhibition of rehydration after the experiment.

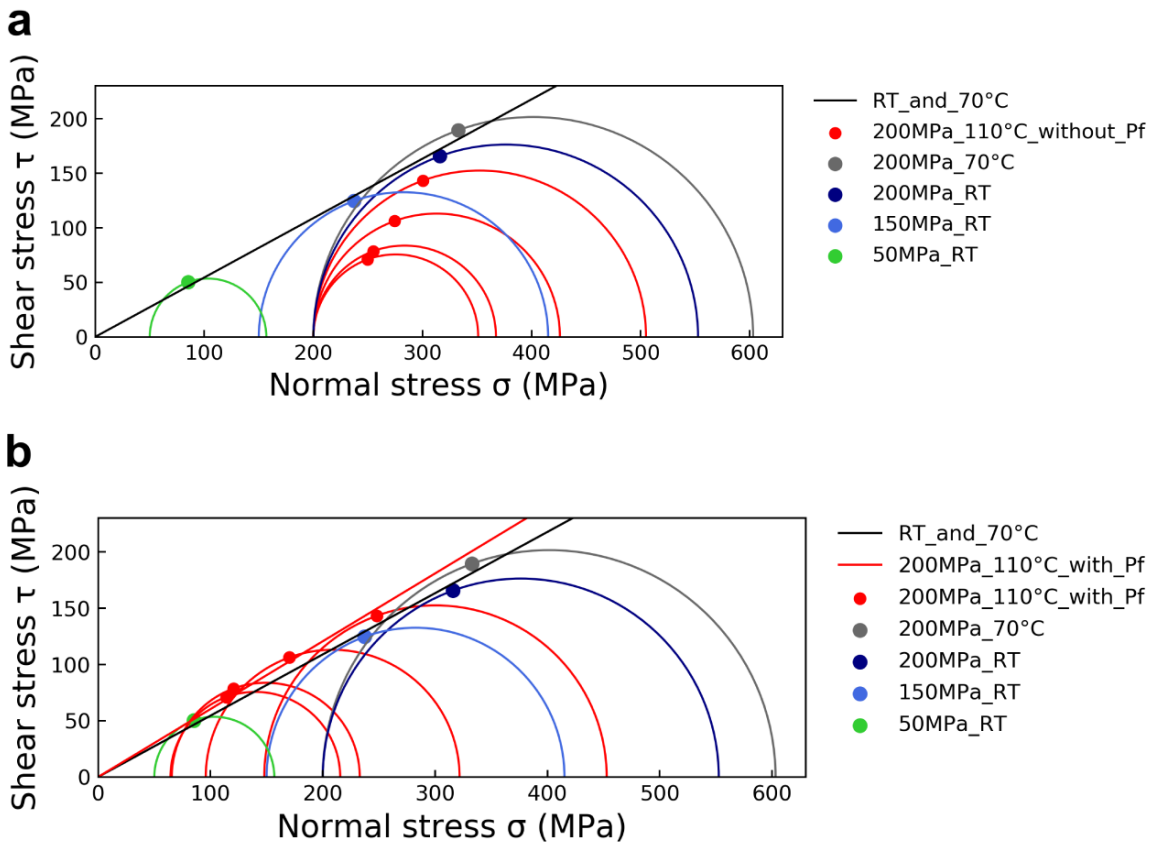

Figure 5. Mohr circle and Mohr-Coulomb yield criterion. We compared frictional coefficient **a** without pore fluid pressure and **b** with pore fluid pressure. First, we plotted Mohr circle and points of normal stress and shear stress, using the data of experimental pressure, differential stress and an axial angle of 35 degrees (see Table S2). Second, we fitted the points of normal stress and shear stress to obtain yield criterion (assuming intercept is 0). The data for RT and 70 °C conditions have a well-fitted yield criterion and the frictional coefficient is 0.54. However, the trend for 200MPa_110°C without pore fluid pressure (red plots in **a**) differs from that for RT and 70 °C conditions. Assuming pore fluid pressure calculated with equation (1) (red plots in **b**), the data for 200MPa_110°C showed a similar trend to the data for RT and 70 °C conditions, and frictional coefficient for 200MPa_110°C became 0.60. The analysis implies that pore fluid pressure occurred during the experiment under 200MPa_110°C

288

289

290 4.2 Time evolution of pore fluid pressure based on Avrami kinetics

291 We calculated effective pressure at each stress drop event by assigning each recurrence
292 interval in equation (1), and plotted pore fluid pressures estimated by the difference between the
293 confining pressure and the effective pressure. In the plotting, we assumed pore fluid pressure was
294 linearly proportional to the volume fraction of transformed material. We used Avrami kinetics
295 (Avrami, 1940) for fitting as follows:

296

$$P_{\mathrm{f}}(t) = A\{1 - \exp(-kt^n)\}, \#(2)$$

297

298 where $P_{\mathrm{f}}(t)$ is pore fluid pressure in MPa and t is elapsed time in s (R^2 = 0.951). Figure 6
299 shows that Avrami equation represents the temporal evolution of pore fluid pressures much more
300 accurately. Notably, that we could not fit the pore pressure evolution by the first order reaction,
301 especially in the middle of the reaction.

302 We obtained two important parameters in Avrami equation: the reaction rate $k = 9.15\times10^{-13}$
303 $s^{-3.72}$ and the exponent $n = 3.72$. According to Arrhenius equation, reaction rate decreases
304 exponentially with the reciprocal of temperature (Logan, 1982; Laidler, 1984), and also,
305 decreases exponentially with pressure (Zhang, 2008). Ballirano and Melis (2009) examined
306 dehydration kinetics of bassanite in air, and their reaction rate was 8.8×10^{-5} s^{-1} at 398 K (the
307 same temperature with our dehydrated condition considering frictional heating (Sibson, 1975)).
308 Our reaction rate obtained under much higher confining pressure is smaller than the value of the
309 previous research, which is consistent with the dependence of reaction rate on pressure and
310 temperature.

311 Regarding Avrami exponent n, we first used the first-order reaction equation (n = 1 in
312 equation 2) as the fitting function. However, we found that Avrami equation (n = 3.72), rather
313 than the first-order reaction equation (n = 1), most accurately represented the time evolution of
314 pore fluid pressures. Therefore, there is a difference of 2.72 in the exponent n between the first-
315 order reaction model and Avrami theory. From the process of deriving Avrami equation, the
316 exponent n becomes the sum of fractal dimension on the surface of reaction products (water and
317 anhydrate) D_s and 1 (i.e., $n = D_s + 1$) (Shimakawa, 2012). Based on this, our fractal dimension on
318 the surface of reaction products becomes 2.72. It is considered that due to the involvement of
319 spatial parameters such as particle shape, a power of time appears in Avrami equation.
320 Additionally, when the fractal dimension 2.72 in space is converted to fractal dimension in the
321 two-dimensional space (2D cross-section) of the Euclidean geometry, the fractal dimension on
322 the surface of reaction products is estimated to be 1.72. This fractal dimension 1.72 represents
323 how water forms a network within the gouge. In other words, since water exists in the pores
324 between the gouge, the fractal dimension 1.72 has information on the pore structure within the
325 gouge. The fractal dimension on the fracture system of Riedel shear planes is known to be about
326 1.6 at the maximum (Hirata, 1989), which is smaller than that of the pore structure, 1.72. This
327 indicates that Riedel shear planes develop in some parts of the pore network, and the difference
328 in fractal dimensions (capacity dimension) on fracture systems between Riedel shear planes and

pore network considered from water network has the information on pore structure originally present in the gouge.

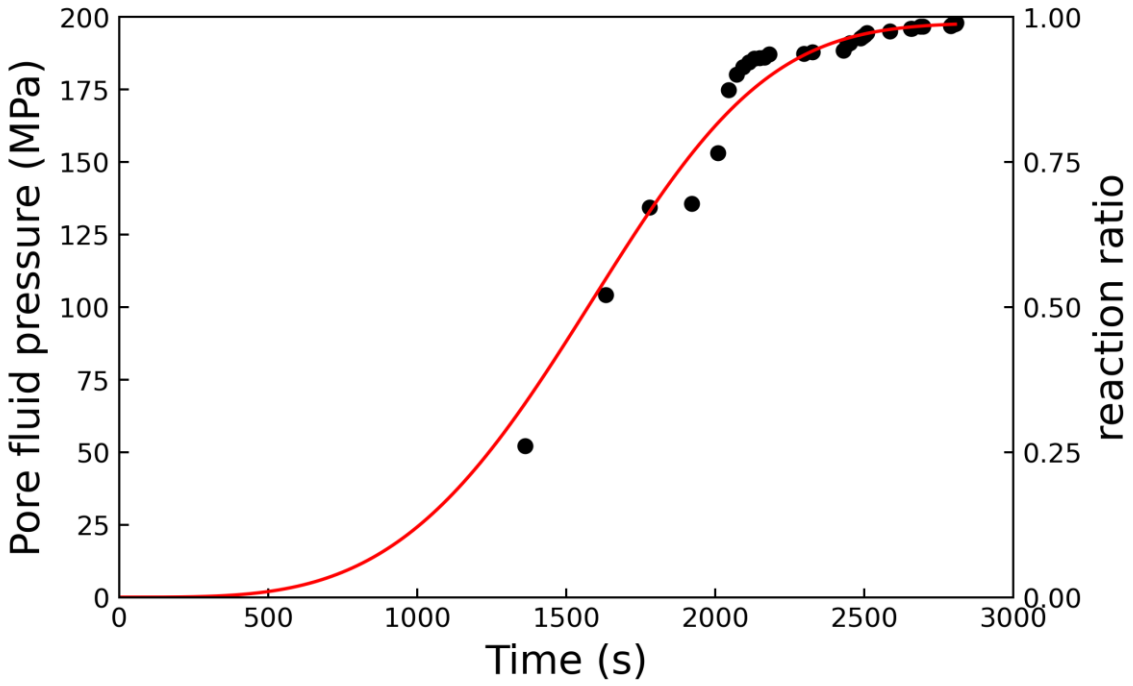

Figure 6. Estimated pore fluid pressure evolution (black dots) and prediction by Avrami equation (red).

4.3 Avrami kinetics and Weibull's fracture progression rates

In addition to the discussion on Avrami exponent, for the obtained function, the time function of pore fluid pressure indicates the kinetically controlled degree of strength reductions, in other words, the fracture progression rate. Moreover, if we view the separation reaction of a substance, such as dehydration reaction, as a destructive process called decomposition, Avrami equation can be regarded as Weibull cumulative distribution function which is often utilized for describing the failure rate. Hence, it is assumed that Weibull cumulative distribution function has a meaning not only of the failure rate but also the fracture progression rate. During our deformation experiment conducted under 200MPa_110°C, four stick-slip events with large stress drops occurred by 1921 s (corresponding to shear strain of about 3.5 in Figure 1b) after the start of the experiment (see Figure S1). By substituting t = 1921 s in equation (2), the reaction ratio was estimated to be approximately 80 %. This indicates that the high reaction progress rate close

to the completion of reaction controls the majority of the fracturing process, supporting that Weibull cumulative distribution function also has a meaning of the fracture progression rate. In other words, large stress drops were induced in the phase of the rapid increase in the reaction ratio where the pore fluid pressure rapidly increased between 1360 and 1921 s in Figure 6 (corresponding to shear strain between 1.9 and 3.5 in Figure 1b). When the reaction progress rate gradually decays where the rate of pore fluid pressure build-up decays after approximately 1921 s in Figure 6 (corresponding to shear strain of about 3.5 or greater in Figure 1b), slip events with small stress drops dominated. This indicates that the reaction rate in Avrami equation also has a meaning of the fracture progression rate via the Weibull function. The rate of increase in pore fluid pressure affects the amount of stress drop, and therefore, we conclude that dehydration kinetics of hydrous minerals control stick-slip behaviors.

5 Conclusions

We conducted deformation experiments using bassanite as an analogue material for dehydrating system and reproduced dehydration instability in the laboratory. We demonstrated the existence of dehydration-derived pore fluid pressure during our deformation experiment under 200 MPa and 110 ℃ from the perspectives of microstructures and mechanical behaviors, and derived the time function of pore fluid pressure based on Avrami kinetics. Moreover, the Avrami equation provided the information on pore structures based on fractal geometry and Weibull cumulative distribution function for the fracture progression rate. The analysis revealed that the amount of slip was controlled by dehydration kinetics of hydrous minerals. The time function of pore fluid pressure evolution derived from laboratory experiments contribute to better understanding of the seismogenesis of deep and intermediate-depth earthquakes.

Data Availability Statements

The data in this study can be found in general repository.
(https://doi.org/10.6084/m9.figshare.25044524.v1)

Acknowledgments

This work was supported by KAKENHI grant number 22H04932 and by the Ministry of Education, Culture, Sports, Science, and Technology (MEXT) of Japan under its Earthquake and Volcano Hazards Observation and Research Program.

References

Avrami, M. (1940), Kinetics of phase change. II Transformation-time relations for random distribution of nuclei. The Journal of Chemical Physics, 8, 212–224. https://doi.org/10.1063/1.1750631

Ballirano, P. & Melis, E. (2009), Thermal behaviour and kinetics of dehydration of gypsum in air from in situ real-time laboratory parallel-beam X-ray powder diffraction. Phys. Chem. Miner. 36, 391–402.

Brantut, N. *et al.* (2012), Dehydration-induced damage and deformation in gypsum and implications for subduction zone processes. *Journal of Geophysical Research,* 117, 1–17. https://doi.org/10.1029/2011JB008730

Chernak, L. J. & Hirth, G. (2011), Syndeformational antigorite dehydration produces stable fault slip. *Geology*, 39, 847–850. https://doi.org/10.1130/G31919.1

Chollet, M., Daniel, I., Koga, K. T., Petitgirard, S. & Morard, G. (2009), Dehydration kinetics of talc and 10 Å phase: Consequences for subduction zone seismicity. Earth and Planetary Science Letters, 284, 57–64. https://doi.org/10.1016/j.epsl.2009.04.008

Freyer, D. & Voigt, W. (2003), Crystallization and Phase Stability of CaSO4 and CaSO4 – Based Salts. Monatshefte für Chemie 134, 693–719. https://doi.org/10.1007/s00706-003-0590-3

Gu, Y. & Wong, T. fong. (1994), Development of shear localization in simulated quartz gouge: Effect of cumulative slip and gouge particle size. PAGEOPH 143, 387–423. https://doi.org/10.1007/BF00874336

Hirata, M., Muto, J. & Nagahama, H. (2014), Experimental analysis on Rowe's stress-dilatancy relation and frictional instability of fault gouges. *Episodes* 37, 303-307. https://doi.org/10.18814/epiiugs/2014/v37i4/010

Hirata, T. (1989), Fractal dimension of fault systems in Japan: Fractal structure in rock fracture geometry at various scales. *PAGEOPH* 131, 157–170.

Hirauchi, K. I. & Muto, J. (2015), Effect of stress state on slow rupture propagation in synthetic fault gouges 4. Seismology. *Earth, Planets and Space*, 67, 25. https://doi.org/10.1186/s40623-015-0199-x

Jayawickrama, E. G., Muto, J., Sasaki, O. & Nagahama, H. (2021), Damage Evolution of Onnagawa Shale by Postmortem Thresholding of X-Ray Computed Tomography. *Journal of Geophysical Research,* 126, 1–22. https://doi.org/10.1029/2021JB022056

Kirby, S. (1995), Interslab earthquakes and phase changes in subducting lithosphere. Reviews of Geophysics, 33, 287–297. https://doi.org/10.1029/95RG00353

Laidler, K. J. (1984), The development of the arrhenius equation. Journal of Chemical Education 61, 494–498. https://doi.org/10.1021/ed061p494

Leclère, H., Faulkner, D., Wheeler, J. & Mariani, E. (2016), Permeability control on transient slip weakening during gypsum dehydration: Implications for earthquakes in subduction zones. *Earth and Planetary Science Letters,* 442, 1–12. https://doi.org/10.1016/j.epsl.2016.02.015

Logan, S. R. (1982), The origin and status of the Arrhenius equation. J. Chem. Educ. 59, 279–281. https://doi.org/10.1021/ed059p279

Milsch, H. H. & Scholz, C. H. (2005), Dehydration-induced weakening and fault slip in gypsum: Implications for the faulting process at intermediate depth in subduction zones. Journal of Geophysical Research, 110, 1–16. https://doi.org/10.1029/2004JB003324

Mirwald, P. W. (2008), Experimental study of the dehydration reactions gypsum-bassanite and bassanite-anhydrite at high pressure: Indication of anomalous behavior of H_2O at high pressure in the temperature range of 50-300 °C. *The Journal of Chemical Physics*, 128, 074502. https://doi.org/10.1063/1.2826321

Olgaard, D. L., Ko, S.-c. & Wong, T. (1995), Deformation and pore pressure in dehydrating gypsum under transiently drained conditions. Tectonophysics, 245, 237–248. https://doi.org/10.1016/0040-1951(94)00237-4

Onuma, K., Muto, J., Nagahama, H. & Otsuki, K. (2011), Electric potential changes associated with nucleation of stick-slip of simulated gouges. Tectonophysics 502, 308–314. https://doi.org/10.1016/j.tecto.2011.01.018

Perrillat, J. P. et al. (2005), Kinetics of antigorite dehydration: A real-time X-ray diffraction study. Earth and Planetary Science Letters, 236, 899–913. https://doi.org/10.1016/j.epsl.2005.06.006

Proctor, B. & Hirth, G. (2015), Role of pore fluid pressure on transient strength changes and fabric development during serpentine dehydration at mantle conditions: Implications for subduction-zone seismicity. Earth and Planetary Science Letters, 421, 1–12.

Raleigh, C. B. & Paterson, M. S. (1965), Experimental deformation of serpentinite and its tectonic implications. Journal of Geophysical Research, 70, 3965–3985. https://doi.org/10.1029/JZ070i016p03965

Scuderi, M. M., Niemeijer, A. R., Collettini, C. & Marone, C. (2013), Frictional properties and slip stability of active faults within carbonate–evaporite sequences: The role of dolomite and anhydrite. Earth and Planetary Science Letters, 369–370, 220–232. https://doi.org/10.1016/j.epsl.2013.03.024

Shimakawa, K. (2012), Dynamics of crystallization with fractal geometry: Extended KJMA approach in glasses. Phys. Status Solidi Basic Res. 249, 2024–2027. https://doi.org/10.1002/pssb.201200347

Shimazaki, K. and Nakata, T. (1980) Time-predictable recurrence model for large earthquakes. *Geophysical Research Letters* 7, 279-282. https://doi.org/10.1029/GL007i004p00279

Shiraishi, R., Muto, J., Tsunoda, A., Sawa, S. & Suzuki. (2022), A. Localized Deformation of Lawsonite During Cold Subduction. Journal of Geophysical Research, 127, e2021JB022134. https://doi.org/10.1029/2021JB022134

Sibson, R. H. (1975), Generation of pseudotachylyte by ancient seismic faulting. *Geophysical Journal of the Royal Astronomical Society* 43, 775–794. https://doi.org/10.1111/j.1365-246X.1975.tb06195.x

Tang, Y., Gao, J., Liu, C., Chen, X. & Zhao, Y. (2019), Dehydration Pathways of Gypsum and the Rehydration Mechanism of Soluble Anhydrite γ-$CaSO_4$. *ACS Omega* 4, 7636–7642. https://doi.org/10.1021/acsomega.8b03476

Yamasaki, T. & Seno, T. (2003), Double seismic zone and dehydration embrittlement of the subducting slab. Journal of Geophysical Research, 108, 1–21. https://doi.org/10.1029/2002JB001918

Zhang, Y. (2008), Geochemical Kinetics, Princeton University Press.